Mn-doped $Co_2(OH)_3Cl$ Xerogels with 3D Interconnected Mesoporous Structures as Lithium Ion Battery Anodes with Improved Electrochemical Performance

Zhiwei Zhang, Longwei Yin*

Key Laboratory for Liquid-Solid Structural Evolution and Processing of Materials, Ministry of Education, School of Materials Science and Engineering, Shandong University, Jinan 250061, P. R. China

Email: yinlw@sdu.edu.cn

Abstract

Considering the merits of 3D mesoporous interconnected structures with large surface area of xerogel and high theoretical capacity of $Co_2(OH)_3Cl$ incorporating simultaneously both chlorine and hydroxyl functional groups, it is of greatly fundamental importance and challenge to tune porous structure, surface area, and functionally doping to enhance the electrochemical performance of $Co_2(OH)_3Cl$ xerogel anodes for lithium ion batteries (LIBs). Herein, we for the first time report Mn-doped $Co_2(OH)_3Cl$ 3D mesoporous xerogels assembled from nanoparticles via one-step sol-gel method. The effect of Mn doping on the microstructures, surface area, charge transfer kinetics, and electrochemical performance of Mn-doped $Co_2(OH)_3Cl$ xerogels are systematically investigated. It is shown that 4%Mn-doped $Co_2(OH)_3Cl$ xerogels display excellent electrochemical performance, showing a superior capacity of 1377 mAh g^{-1} after 50 cycles at a current density of 100 mA g^{-1}. Even when the current density increases to 1600 mA g^{-1}, it still maintains the capacity of 824 mAh g^{-1}. The great enhancement on electrochemical performance can be mainly due to the uniquely special 3D hierarchically porous interconnected xerogel structure with high surface area, the enhancement of the electric conductivity and charge transfer kinetics, and the activated redox reaction kinetics related to LiOH and LiCl for the Mn-doped $Co_2(OH)_3Cl$ xerogels.

1. Introduction

Transition metal oxides (M_xO_y, M = Co,[1-3] Ni,[4-6] _ENREF_1 Mn[7-10] and Cu[11-13]) have attracted much attention as alternative anode materials for lithium ion batteries (LIBs) because of their higher lithium storage capacity than that of graphite (< 372 mAh g^{-1}). The redox reactions taken place during delithiation/lithiation process for M_xO_y LIBs anodes are associated with the formation of nano-sized metal particles and Li_2O. In the reverse process, metallic nanoparticle and Li_2O can be oxidized into oxides. The lithiation/delithiation redox process for transition metal hydroxide LIBs anodes are associated with the reaction between hybdroxides and lithium to form LiOH and metal nanoparticle. Maybe due to an anxiety about "hydrogen" of hydroxides, transition-metal hydroxide LIBs anodes are first time reported until 2010.[14] After that, metal hydroxides such as $Co(OH)_2$ and $Ni(OH)_2$ are attracting much attention for their layered structure with large interlayer spacing and well-defined electrochemical redox activity as LIBs anodes. Nevertheless, large volume changes generated during the lithiation/delithiation processes and poor electronic conductivity hinder the improvement of electrochemical performance of metal hydroxide LIBs anodes.[14,15] More recently, metal chlorides, such as $CoCl_2$, AgCl, $CuCl_2$,[16,17] are attracting much attention for their potential application as alternative LIBs anodes. The weaker bonding between metal and chlorine species may be kinetically favorable for the redox conversion reaction, giving a large multi-electron redox capacity.[18] It should be expected that the metal-based materials simultaneously incorporating both the chlorine and hydroxyl functional groups can display a superior electrochemical performance due to the redox reaction related to LiOH and LiCl.[19]

$Co_2(OH)_3Cl$ is a solid solution of $Co(OH)_2$ and $CoCl_2$. A possible electrochemical reaction process of $Co_2(OH)_3Cl$ with Li can be described as follows:

$$CoCl_2 + 2Li^+ + 2e^- \Leftrightarrow Co + 2LiCl \quad \text{and}$$
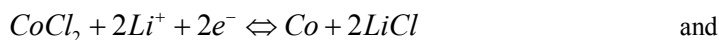
$$Co(OH)_2 + 2Li + 2e^- \Leftrightarrow Co + 2LiOH$$

.[20,21] $Co_2(OH)_3Cl$ has a pyrochlore-like hexagonal structure with unit cell constants of a = 6.8420 Å, c = 14.504 Å, comprises a close packing of $(OH)_3Cl$ in which Co^{2+} occupies the octahedral sites.[22,23] The formula of $Co_2(OH)_3Cl$ is firstly established by Feitkneeht in 1935 for the lavender-colored cobalt hydroxyl chloride.[24-28] $Co_2(OH)_3Cl$ can accommodate 4 Li$^+$ ions per formula unit, possessing a theoretical specific capacity of 525 mAh g^{-1}. To improve the electrochemical performance, such as lithium storage capacity, rate capability and cycle stability of $Co_2(OH)_3Cl$ anodes, one of the strategies is to incorporate metal ions into lattice of $Co_2(OH)_3Cl$, efficiently increasing the electric conductivity and enhancing charger transfer kinetics at the interface between the anodes and electrolytes. Another strategy is to design rationally large-surface area nanostructured $Co_2(OH)_3Cl$ electrodes

with porous structure to alleviate the volume changes and stress, providing more space for electrolyte diffusion, shorten the diffusion route.

As a kind of novel porous materials with merits of continuous porosities, high surface areas, and interconnected three-dimensional (3D) structure, xerogel oxide is being paid much attention as promising materials for electrodes for LIBs and supercapacitors, advanced catalyst supports, adsorbents, and a variety of other applications.[29-31] For example, Reddy's study suggests that MnO_2 xerogel electrodes display an enhanced electrochemical supercapacitor performance, reaching a maximum capacitance of 130 F g^{-1}.[32] Especially, as anode materials for LIBs, the uniquely 3D porous structure of oxide xerogel can provide a high surface area, large surface to volume ratio, and interconnected hierarchically porous structure, thus leading to relatively short ion and charge diffusion pathways and high transport rates of both lithium ions and electrons.[32] It is reported that V_2O_5 xerogel LIBs anodes display the ability to intercalate lithium reversibly, showing improved lithium storage capacity compared to other types of V_2O_5 nanostructured materials.[33-35] Recently, it is shown that oxide xerogels assembled from nanocrystalline particles with abundant mesopores can exhibit excellent cycling performance and rate capability as LIBs anodes.[37-38] Considering the advantages of 3D porous xerogel structured materials with large surface area and high theoretical capacity of $Co_2(OH)_3Cl$ incorporating simultaneously both the chlorine and hydroxyl functional groups, it is of great importance and challenge to tune the porous structure, surface area, and functionally doping to enhance the electrochemical performance of $Co_2(OH)_3Cl$ xerogel materials.

Herein we for the first time report Mn-doped $Co_2(OH)_3Cl$ mesoporous xerogels assembled from nanocrystalline particles via one step sol-gel method, as anode material for LIBs with outstanding electrochemical performance. The effects of Mn doping on the microstructures, surface area, charge transfer kinetics at the anode interface, and electro chemical performance of Mn-doped $Co_2(OH)_3Cl$ mesoporous xerogels are systematically investigated. It is shown that 4%Mn-doped $Co_2(OH)_3Cl$ xerogels display superior electrochemical performance, showing a superior capacity of 1377 mAh g^{-1} after 50 cycles at a current density of 100 mA g^{-1}. Even as the current density increases to 1600 mA g^{-1}, it still maintains the capacity of 824 mAh g^{-1}.

2．Experimental section

2.1 Preparation of the $Co_2(OH)_3Cl$ and Mn-doped $Co_2(OH)_3Cl$ samples

Firstly, $CoCl_2·6H_2O$ is used as the precursors and dissolved in mixed solution of ethanol and deionized water, followed by addition of propylene oxide at a propylene oxide/metal-ion in a molar ratio of 10:1. The solution is stirred for 30 min and then left still to gel at room temperature for 1 h. To remove the by-products from the pore structure of the wet gel, the wet gel is then

washed with ethanol for three times and subsequently dried at 353 K for 6 h in a vacuum oven. The dried xerogel products are further calcined at 473 K for 5 h to improve the crystalline state of the products. For the preparation of Mn-doped $Co_2(OH)_3Cl$ xerogel, the $MnCl_2 \cdot 4H_2O$ is used as the Mn source precursor. The sol-gel forming process of $Co_2(OH)_3Cl$ xerogels is demonstrated in Schema S1 in supporting information.

2.2 Sample characterization

The powder x-ray diffraction (XRD) patterns of the products are determined by Rigaku D/Max-KA diffractometer equipped with Cu Ka radiation. The morphology and chemical components of the products are analyzed using SU-70 field emission scanning electron microscopy (FE-SEM). The microstructures of the synthesized products are analyzed using high-resolution transmission electron microscopy (HR-TEM) of JEM-2100 at an acceleration voltage of 200 kV. Nitrogen adsorption-desorption isotherms are determined at 77 K using micromeritics ASAP 2020 surface area and porosity analyzer. The surface area parameters are calculated according to the Brunauer-Emmett-Teller (BET) method. The pore size distribution is obtained from the desorption branch of isotherm using the corrected form of Kelvin equation by means of the Barrett-Joyner-Halenda (BJH) method. XPS spectra are measured and collected using a 632.8 nm laser with a JY HR800 under ambient condition, with a laser spot size of about 1 μm. X-ray photoelectron spectroscopy (XPS) characterization is carried out in an ESCALAB 250 instrument with 150W Al Ka probe beam. Survey and multiregion spectra were recorded at Cl 2p, Co 2p, Mn 2p, C1s and O 1s peaks.

2.3 Electrochemical measurements

Working electrodes are prepared by mixing 75 wt% active material of x%Mn-$Co_2(OH)_3Cl$, 15 wt% acetylene black (Super-P), and 10 wt% polyvinylidene fluoride binder dissolved in N-methyl-2-pyrrolidinone. The galvanostatic charging/discharging tests are conducted using standard 2025 type coin cells with copper foil as the current collector, lithium foil as reference electrodes and 1.0 M $LiPF_6$ in mixed ethylene carbonate (EC) and diethyl carbonate (DEC) (EC:DEC, 1:1 by volume) as the electrolyte. A cut-off voltage window of 0.01 – 3.0 V is used. The 2025 coin-type cells are assembled in an argon-filled glovebox with less than 1 ppm of oxygen and water, galvanostatically cycled on a LAND CT2001A instrument (Wuhan, China) at room temperature. Cyclic voltammetry (CV) study is conducted using an electrochemical workstation (PARSTAT 2273) between 0.01-3.0 V at a scan rate of 0.1 mV s^{-1}.

3. Results and Discussion

$Co_2(OH)_3Cl$ exhibits a deformed pyrochlore structure regarded as a solid solution of $Co(OH)_2$ and $CoCl_2$, corresponding to a hexagonal crystal structure with a space group of R-$3m$, with lattice

constants of a = 6.8420 Å, c = 14.504 Å (PDF no. 166). [27] Figure 1 depicts the 3D structure model of $Co_2(OH)_3Cl$. As shown in Fig. 1a, the Co^{2+} displays two types of chemical bonding of Co-Cl and Co-OH related to $CoCl_2$ and $Co(OH)_2$, respectively. A deformed octahedral can be revealed and the Co^{2+} occupies vertex and body center sites (Fig. 1b), which is comprised of two tetrahedras. By changing the orientation, the bonding of Co-O and Co-Cl in the deformed octahedral is presented in the Fig. 1c. The Co-Co distance on one side of the tetrahedron near Cl is 3.42 Å, whereas those on the other three sides bonded by OH are 3.12 Å, and Co ions form tetrahedra with three OH and one Cl near the four sides.

3.1 XRD

Fig. 2a shows the typical X-ray diffraction patterns of the pure $Co_2(OH)_3Cl$ and Mn-doped $Co_2(OH)_3Cl$ xerogels with different Mn doping content of 0, 2%, 4%, 8%, respectively. The major diffraction peaks of (101), (113), and (024) correspond to that of rhombohedral $Co_2(OH)_3Cl$ (JCPDS. 73-2134). [20,33] With Mn doping content increasing, no impurity phases are detected from the XRD patterns, indicating that Mn enters into the lattice of $Co_2(OH)_3Cl$, with a slight shift to position at larger angles for all diffraction peaks. To further determine the effect of Mn doping on the crystal structure of $Co_2(OH)_3Cl$, the magnified main (101) peak is given in Fig. 2b. Because of the smaller radius of Mn^{4+} (0.53 Å) than that of Co^{2+} (0.545 Å), when Co^{2+} is partially replaced by Mn^{4+}, the lattice constants and planar inter-spacing (d) become smaller. [34] According to Bragg equation of $2dsin\theta = n\lambda$, the incorporation of Mn induces a slight shift for the diffraction peaks to positions at larger angles. In the present case, the inter-planar spacing of (101) the 4%Mn-$Co_2(OH)_3Cl$ xerogel is estimated to be 5.4728 Å (a = 6.825 Å, c=14.499 Å), smaller than d-spacing of 5.4854 Å of (101) plane for $Co_2(OH)_3Cl$.

3.2 XPS

X-ray photoelectron spectroscopy (XPS) measurements are carried out to determine the chemical composition and chemical bonding state of 4%Mn-$Co_2(OH)_3Cl$ xerogel (Fig. 3a). The survey XPS spectrum for the sample is shown in Fig. 3a, indicating the presence of Mn, O, Co, Cl and C elements. The C peak is attributed to the residual carbon from the sample and adventitious hydrocarbon from the XPS instrument itself. According to the handbook of XPS, the binding energy of 531.8 eV for O 1s (Fig. S1 in supporting information) can be mainly derived from the combination of hydroxyl group (O-H) with a binding energy of $\sim$531 eV. [35] The two different peaks in Fig. 3b can be associated with Cl 2p in the $(OH)_3Cl$ group. [36] In Fig. 3c, the Co 2p XPS spectrum of the sample exhibits two peaks at 782.4 and 797.9 eV, corresponding to the characteristic peaks of Co $2p_{3/2}$ and Co $2p_{1/2}$, respectively, the other two weak peaks at 787.2 and 804.2 eV belong to the shake-up satellite peaks of the above two peaks, demonstrating the presence of Co^{2+}. [37] Fig. 3d exhibits the high-resolution Mn $2p_{3/2}$ and Mn $2p_{1/2}$ peaks centered at

642.2 and 654 eV with satellite peaks, respectively, with a spin-energy separation of 11.8 eV, in good agreement with reported data of Mn^{4+}.[38]

3.3 SEM & BET

Fig. 4a shows a typical SEM image of the 4%Mn-$Co_2(OH)_3Cl$ xerogel. As shown in Fig. 4a, the prepared xerogel products display a three-dimensional interconnected porous skeleton characteristic architecture. The synthesized xerogels are composed of nanoparticles, which connect with each other to form 3D mesoporous xerogel with a high surface area. The size of Mn doped $Co(OH)_2Cl_3$ crystal particles can be observed from the Fig. 4a. Such unique 3D interconnected porous structures can lead to relatively short ion and charge diffusion pathway and high transport rates for both lithium ions and electrons. The typical EDX element mapping images in Fig. 4c-4f suggest that the sample is composed of O, Cl, Co, Mn elements, showing that all species are homogeneously distributed among the area in Fig. 4b.

Fig. 5 gives nitrogen adsorption-desorption isotherms and the corresponding pore size distribution curves of $Co_2(OH)_3Cl$ and 4%Mn-$Co_2(OH)_3Cl$ xerogels. They exhibit a typical type IV isotherm with a H1 hysteresis loop (Fig. 5a), indicating a disordered mesoporous structure for the $Co_2(OH)_3Cl$ and 4%Mn-$Co_2(OH)_3Cl$ xerogels. The broad distribution of 2-50 nm (Fig. 5b) of the xerogel samples confirms the presence of abundant mesopores. The $Co_2(OH)_3Cl$ sample displays a BET surface area of 92.4 $m^2 g^{-1}$ and average pore size of 33.36 nm. With Mn ions incorporated into lattice of $Co_2(OH)_3Cl$ sample, the BET surface area and pore size of 4%Mn-$Co_2(OH)_3Cl$ xerogel samples change to 117.32 $m^2 g^{-1}$ and 33.64 nm, respectively. From Table S1, it can be revealed that with Mn doping concentration increasing, the BET surface area, and pore volume increase. Fig. S3 depicts a TEM image of 0% Mn doped $Co_2(OH)_3Cl$ sample, showing an average size of 10-12 nm for the $Co_2(OH)_3Cl$ nanoparticles. It shows a larger diameter for the 0% Mn doped $Co_2(OH)_3Cl$ sample than 4% Mn-doped $Co_2(OH)_3Cl$. It is generally believed that the smaller crystallite size can increase the surface area.[39a]

According to nitrogen adsorption-desorption isotherms, the surface area, pore diameter and pore volume increase after Mn doping. In fact, many factors such as crystal size, particle distribution, etc. have influences on pore volume and pore diameter, so the reasons for pore volume changes are often complicated. According to previous works, smaller crystals often lead to higher pore volumes, which is consistent with our results.[39b,c]

3.4 TEM

Fig. 6a and 6b depict low- and high-magnification TEM images of the 4%Mn-$Co_2(OH)_3Cl$ xerogels. It is indicated that the xerogel sample is composed of nanoparticles with an average size of 10 nm, and shows a characteristic of interconnected structure with nanoparticles homogeneously dispersed and connected each other, forming the typical gel skeleton architecture.
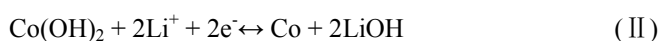
The microstructure of the xerogel can be further revealed by high resolution TEM (HRTEM) lattice image (Fig. 6c) and selected area electron diffraction (SAED) pattern (Fig. 6d). The well-ordered lattice fringe with a spacing of 0.44 nm can be well assigned to d-spacing of (012) plane of $Co_2(OH)_3Cl$ (Fig. 6c). The diffraction rings from SAED pattern in Fig. 6d are in good agreement with that of (021), (202), (205), (220),(134) and (226) planes of $Co_2(OH)_3Cl$ phase.

For the information on chemical composition component and species distribution of the 4%Mn-$Co_2(OH)_3Cl$ xerogel, EDX mapping analysis is further carried out in an energy dispersive x-ray spectrometer (EDX) attached in TEM. Fig. 7d is a typical EDX spectrum from the synthesized products. The EDX mapping images of Co, O, Mn, and Cl elements in Fig. 7b-7c and 7e-7f for the 4%Mn-$Co_2(OH)_3Cl$ sample, suggesting the component species are homogeneously distributed in the area in Fig. 7a.

3.5 Electrochemical performances

For a better understanding of the redox reaction mechanism of the Mn-doped $Co_2(OH)_3Cl$ xerogels as LIBs anodes, the electrochemical performance is evaluated using various electrochemical measurements. Cyclic voltammograms (CV) profiles are shown in Fig. 8a-8c. The reversible electrochemical reaction process can be described as follows:[14,17,20]

$$CoCl_2 + 2Li^+ + 2e^- \leftrightarrow Co + 2\ LiCl \qquad\qquad (\text{I})$$

$$Co(OH)_2 + 2Li^+ + 2e^- \leftrightarrow Co + 2LiOH \qquad\qquad (\text{II})$$

In the first cycle, two main reduction peaks at 0.8, 1.03 and 1.31 V, one reduction weak peak at near 0 V, can be clearly observed, respectively. Due to 15% acetylene black is supplemented to the active material, one peak near 0 V can be detected. At the first cycle, the reduction peak to form LiCl should appear at the peak of 1.3 V, and the peak at 1.03 V may be due to the Li ion insertion to $Co(OH)_2$ to form LiOH. The reduction peak at 0.8 V is ascribed to the decmposition of electrolyte with the formation of solid electrolyte interphase (SEI). After the first cycle, the peak at 1.3 V shifts to the position with higher potential ~ 1.6 V and the peak at 1.03 V shifts to position at lower potential 0.75 V with increasing in cycle number. Meanwhile, the peak at 0.8 V disappears, which can be due to the irreversible formation of SEI films on the surface of electrode. It should be also noted that with the Mn doping content increasing, the current intensity of the reduction peaks at 0.8 and 1.3 V becomes stronger, revealing a fast kinetics for the phase transformation of $Co(OH)_2$ and $CoCl_2$ and the formation of the SEI film. It is also worth noting that with the Mn content increasing, the intensity of the cathodic and anodic peaks of the Mn doped $Co_2(OH)_3Cl$ xerogels, gets stronger, as shown in Fig. 8a-8c, indicating electrochemical activity improvement of the Mn-doped $Co_2(OH)_3Cl$ electrodes. Such an electrochemical activity improvement can be attributed to the Mn incorporation into lattice of $Co_2(OH)_3Cl$, which enhances the charge transfer kinetics at interface between anodes and electrolyte. The

7

4%Mn-$Co_2(OH)_3Cl$ xerogel displays a larger integral area in the CV curves, resulting from improved kinetics process of the transformation of LiOH, LiCl and Li_2O and less irreversible capacity losses.[40,41]

The oxidation peaks at 1.4 V and 2.3 V in the anodic process correspond to the reversible oxidation of Co to Co^{2+}. The 1.4 V peak is ascribed to the transformation from Co to $Co(OH)_2$, and the 2.3 V peak is owing to the oxidation process of Co to $CoCl_2$.[20] In addition, one pair of inconspicuous redox peaks appearing at 2.7 and 1.56 V for the 4%Mn-$Co_2(OH)_3Cl$ sample, is due to the absorption/desorption of lithium ions at the electrode surface and Li^+ insertion/extraction process, which agrees well with the previous reports.[42-44] From the second cycle, the two pairs of reversible redox peaks almost overlap, indicating a good cyclability for the Mn-doped $Co_2(OH)_3Cl$ xerogel electrodes.

As shown in Fig. 8d-8f, the charge and discharge curves of the x%Mn-$Co_2(OH)_3Cl$ LIBs anode samples with different Mn doping contents are investigated in the voltage plateau of 0-3 V versus Li/Li^+ at a current density of 100 mA g^{-1}. The first discharge curve displays three slopes at 1.5-1.0, 1.0-0.8 and 0.8-0.1 V, corresponding to the initial three cathodic peaks during CV process described in Fig. 8a-8c, respectively. With the increase of Mn content incorporated, the first discharge capacity changes from 1796 to 1966 and 1510 mAh g^{-1} for 2%, 4%, 8% Mn-doped $Co_2(OH)_3Cl$ samples, while the charge capacity changes from 1239 to 1588 and 1183 mAh g^{-1}, corresponding to a Coulombic efficiency of 69.0%, 80.8% and 78.4%, respectively. The irreversible capacity during the first cycle is mainly due to the formation of SEI film. At the 20th cycle, 4%Mn-$Co_2(OH)_3Cl$ xerogel sample shows discharge capacity of 1368 mAh g^{-1}, while the discharge capacity at the 10th cycle is 1393 mAh g^{-1}. The capacity loss is only 25.3 mAh g^{-1} from the 10th to the 20th cycle, corresponding to 1.8%.

Fig. 9a presents the cycling performances of x% Mn-doped $Co_2(OH)_3Cl$ samples at a current density of 100 mAg^{-1}. It is clearly shown that the capacity of the 0%, and 2% Mn-$Co_2(OH)_3Cl$ sample decreases drastically with cycle time increasing, and the capacity retained is only 277 and 640 mAh g^{-1} after 50 cycles due to the significant volume variation of electrode pulverization during the discharge-charge process. Although 8% Mn-$Co_2(OH)_3Cl$ keeps an uptrend until the 43th cycle, the capacity only remains at 1167 mAh g^{-1} after 50 cycles. While the 4% Mn-$Co_2(OH)_3Cl$ displays a steady capacity at 1377 mAh g^{-1} after 50 cycles, showing a great improvement for the capacity retention and superior cyclability with little capacity fading, with a Coulombic efficiency of 99.6% after 50 cycles.[45-46]

The reversible capacity of 4% Mn-$Co_2(OH)_3Cl$ (1377 mAh g^{-1}) after 50 cycles is considerably higher than the theoretical capacity of pure $Co_2(OH)_3Cl$ (525 mA h g^{-1}). The reason can be explained from the following aspects. It was reported that pseudo-capacitive charge and the

higher-oxidation-state products are jointly responsible for the large additional capacity of cobalt based electrode material. For example, Cao et al. reported a reversible capacity of 1248.8 mA h g^{-1} for the CoO nanostructurd LIBs anodes, even though the theoretical capacity of CoO is only 716 mAh g^{-1}.[47] Similar results are also reported in other cobalt based anodes, we list them in the following table.[48,49]

As one kinds of specially porous structured materials, aerogel and xerogel display typical hierarchically porous structures, with individual nanostructures interconnected each other to form the three-dimensional structures. Mn doped $Co_2(OH)_3Cl$ Xerogel is composed of nanoparticles, connecting each other to form 3D network structure with high surface area and porous.[50] Porous structures with high surface area can provide more space, alleviating the volume changes and stress during the lithiation and delithiation process, facilitating ion transport by providing a smaller resistance and shorter diffusion pathways. Furthermore, Mn doping can effectively improve the charge transfer kinetics at interface between anode and electrolyte.[51] So the capacity of Mn-doped $Co_2(OH)_3Cl$ in the paper is higher than that of theoretical specific capacity. Similar phenomena are ever reported.[47-51]

As for the rate performance of the xerogels, it can be revealed from Fig. 9b. The current density is set from 100, 200, 400, 800 to 1600 mAg^{-1}, then back to 100 mA g^{-1}. It is shown that after 20 cycles at a current density of 200 mAg^{-1}, the Mn-doped $Co_2(OH)_3Cl$ xerogels show the reversible capacity of 515, 897, 1506 and 1072 mAh g^{-1} for 0, 2, 4 and 8%Mn-$Co_2(OH)_3Cl$ samples. When the current density reaches 1600 mAg^{-1}, the capacity of 4%Mn-$Co_2(OH)_3Cl$ xerogel even retains 824 $mAhg^{-1}$, while a capacity of 63.5, 140.6 and 381 $mAhg^{-1}$ can be maintained for the 0, 2% and 8%Mn-$Co_2(OH)_3Cl$ xerogel samples, respectively. After the current density returns back to 100 mA g^{-1}, the discharge capacity of 4%Mn-$Co_2(OH)_3Cl$ increases to 1401 $mAhg^{-1}$, which is almost 2.3 times higher than the capacity of 609 $mAhg^{-1}$ for $Co_2(OH)_3Cl$ sample. The 2%Mn-$Co_2(OH)_3Cl$ and 4%Mn-$Co_2(OH)_3Cl$ sample shows a capacity of 845 and 1041 $mAhg^{-1}$ as the current density is back to 100 mA g^{-1}. The remarkable rate performance suggests that the greater improvement of electrochemical performance for the 4%Mn-$Co_2(OH)_3Cl$ xerogel.[52]

The good electrochemical performance of $Co_2(OH)_3Cl$ samples can be related to the uniquely structure of $Co_2(OH)_3Cl$ incorporating simultaneously both the chlorine and hydroxyl functional groups. Park et al. ever proved that the electric conductivity of metal hydroxy chloride is superior to that of metal oxide and metal chloride hydrates.[20] The similar result can be found from Shu's study on PbOHCl anodes for Li-ion battery.[53] To further understand the superior electrochemical performance of Mn-doped $Co_2(OH)_3Cl$ xerogels as LIBs anode materials, electrochemical impedance spectrum (EIS) (Fig. 10) can reveal the charge transport kinetics at anode interface between the anode and the electrolyte of the xerogel anode samples. As is known, the diameter of the semicircle on Zre axis provides an approximate indication of the charge transfer resistance (Rct).[54] In Fig. 10, the diameter of semicircle of 4%Mn-$Co_2(OH)_3Cl$ sample displays the smaller vale compared with that of $Co_2(OH)_3Cl$, demonstrating the lower resistance of charge-transfer at

interface between the anode and the electrolyte, which can be attributed to the incorporation of Mn ions into lattice of $Co_2(OH)_3Cl$. The semicircle arc of 8% Mn sample is larger than that of 4%, indicating a higher resistance of charge transfer at the electrode/electrolyte interface. Xu et al. reported a similar result for the that the polarization resistance is the smallest for 5% Mn dopd V_2O_5 and the largest for the Mn dopd V_2O_5 samples.[55] Moreover, the EIS spectra after 30 cycles for 4% and 8% Mn doped samples are provided in the supporting information (Fig. S4), showing smaller charge transfer resistance of 4% Mn doped sample than that of 8% Mn doped sample. The electrochemical impedance spectra are composed of the high-frequency semicircle and the straight line in low frequency region. Among these two parts, the high-frequency semicircle represents the charge transfer resistance at the electrode/electrolyte interphase, which is closely related to the electrochemical performance.[56] The equivalent circuit model of this cell system is added in Fig. S4, where Rs is the ohmic resistance of the electrolyte, membrane and electrode, corresponding to the high frequency intercept of the semicircle with the horizontal axis, CPE is constant phase element resistance and Rct represents the charge-transfer resistance corresponding to the semicircle. And Zw is the Warburg impedance arising from the diffusion of Li^+ ions in electrode, corresponding to the inclined straight line in low frequency. After 30 cycles, the semicircle arcs at high frequency are larger than before cycling. It may result from the formation of SEI film, which is not conducive to the charge transfer and Li ion diffusion at the interface of the electrode/electrolyte.[57-58]

The electrochemical performance enhancement of the Mn-doped $Co_2(OH)_3Cl$ xerogel LIBs anodes can be ascribed to the following several aspects: (1) The xerogel structured anodes with a uniquely special 3D porous interconnected structure with high surface area, can shorten the length of the transport of Li ion and electron, and effectively buffer the volume change in the lithiation/delithiation process. (2) $Co_2(OH)_3Cl$ is a solid solution of $Co(OH)_2$ and $CoCl_2$, simultaneously incorporating both the chlorine and hydroxyl functional groups, can display a superior electrochemical performance due to the redox reaction related to LiOH and LiCl, possessing the merits of both the high theoretical capacity of $Co(OH)_2$ and good cycling stability of $CoCl_2$. (3) EIS result suggests that a proper doping content of Mn can improve the charge transfer kinetics at the electrode/electrolyte interface. (4) The incorporation of Mn doping into lattice of $Co_2(OH)_3Cl$ can induce an increase of the BET surface area, the pore diameter and pore volume for Mn-doped $Co_2(OH)_3Cl$ xerogels.

4. Conclusion

We successfully synthesized Mn-doped $Co_2(OH)_3Cl$ xerogels as a novel anode material for LIBs via a facile one pot sol-gel process. The prepared product displays a 3D interconnected hierarchically porous skeleton characteristic architecture. The synthesized xerogels are assembled from nanoparticles connecting each other to form 3D mesoporous structures with a high surface area. Such unique 3D interconnected porous xerogel structures can lead to relatively short ion and charge diffusion pathway and high transport rates for both lithium ions and electrons. The

4%Mn-doped Co$_2$(OH)$_3$Cl xerogel shows the better cycling stability and rate performance compared with pure Co$_2$(OH)$_3$Cl and other x%Mn-doped Co$_2$(OH)$_3$Cl xerogel samples, which can be ascribed to the synergistic effect of high theoretical capacity of Co$_2$(OH)$_3$Cl and high surface area of xerogel with 3D porous interconnected structure. In addition, Mn doping into lattice of Co$_2$(OH)$_3$Cl can induce a increase of the electric conductivity and charge transfer ability, the BET surface area, the pore diameter and pore volume for Mn-doped Co$_2$(OH)$_3$Cl xerogels, makes a significant contribution to the excellent electrochemical performance.

References

[1]   X. W. Lou; D. Deng; J. Y. Lee; J. Feng; L. A. Archer: *Adv. Mater.* **2008**, *20*, 258-262.

[2]   Z.-S. Wu; W. Ren; L. Wen; L. Gao; J. Zhao; Z. Chen; G. Zhou; F. Li; H.-M. Cheng: *ACS Nano* **2010**, *4*, 3187-3194.

[3]   C. Peng; B. Chen; Y. Qin; S. Yang; C. Li; Y. Zuo; S. Liu; J. Yang: *ACS Nano* **2012**, *6*, 1074-1081.

[4]   Y. J. Mai; S. J. Shi; D. Zhang; Y. Lu; C. D. Gu; J. P. Tu: *J. Power Sources* **2012**, *204*, 155-161.

[5]   H. Liu; G. Wang; J. Liu; S. Qiao; H. Ahn: *J. Mater. chem.* **2011**, *21*, 3046-3052.

[6]   X. H. Huang; J. P. Tu; C. Q. Zhang; F. Zhou: *Electrochim. Acta* **2010**, *55*, 8981-8985.

[7]   K. Zhong; X. Xia; B. Zhang; H. Li; Z. Wang; L. Chen: *J. Power Sources* **2010**, *195*, 3300-3308.

[8]   L. Hu; Y. Sun; F. Zhang; Q. Chen: *J.   Alloy Compd.* **2013**, *576*, 86-92.

[9]   G. Yang; Y. Li; H. Ji; H. Wang; P. Gao; L. Wang; H. Liu; J. Pinto; X. Jiang: *J. Power Sources* **2012**, *216*, 353-362.

[10] Y. S. Yun; J. M. Kim; H. H. Park; J. Lee; Y. S. Huh; H.-J. Jin: *J. Power Sources* **2013**, *244*, 747-751.

[11] J. C. Park; J. Kim; H. Kwon; H. Song: *Adv. Mater.* **2009**, *21*, 803-807.

[12] L. Wang; H. Gong; C. Wang; D. Wang; K. Tang; Y. Qian: *Nano scale* **2012**, *4*, 6850-5.

[13] S. Ko; J. I. Lee; H. S. Yang; S. Park; U. Jeong: *Adv. Mater.* **2012**, *24*, 4451-6.

[14] Y.-S. He; D.-W. Bai; X. Yang; J. Chen; X.-Z. Liao; Z.-F. Ma: *Electrochem. Commun.* **2010**, *12*, 570-573.

[15] Y. Yang; W. Xu; R. Guo; L. Liu; S. Wang; D. Xie; Y. Wan: *J. Power Sources* **2014**, *269*, 15-23.

[16] T. Li; Z. X. Chen; Y. L. Cao; X. P. Ai; H. X. Yang: *Electrochim. Acta* **2012**, *68*, 202-205.

[17] J.-l. Liu; W.-j. Cui; C.-x. Wang; Y.-y. Xia: *Electrochem. Commun.* **2011**, *13*, 269-271.

[18] P. G. Bruce; B. Scrosati; J. M. Tarascon: *Angew. Chem.Int. Ed.* **2008**, *47*, 2930-46.

[19] J. Shu; R. Ma; L. Shao; M. Shui; L. Hou; K. Wu; Y. Chen; D. Wang; Y. Liang; Y. Ren: *RSC Adv.* **2013**, *3*, 372.

[20] G. D. Park; Y. N. Ko; Y. C. Kang: *Sci. Rep.* **2014**, *4*, 5785.

[21] J. J. Ma; T. Yuan; Y.-S. He; J. Wang; W. Zhang; D. Yang; X.-Z. Liao; Z.-F. Ma: *J. Mater. chem. A* **2014**, *2*, 16925-16930.

[22] X. G. Zheng; M. Hagihala; M. Fujihala; T. Kawae: *J. Phys.: Conf. Ser.* **2009**, *145*, 012034.

[23] M. Hagihala; X. G. Zheng; T. Kawae: *Physica B: Condensed Matter* **2009**, *404*, 671-673.

[24] M. Fujihala; M. Hagihala; X. G. Zheng; T. Kawae: *Phys. Rev. B.* **2010**, *82*.

[25] Z. Zhao; F. Geng; J. Bai; H.-M. Cheng: *J. Phys. Chem. C* **2007**, *111*, 3848-3852.

[26] P.M. de WOLFF; Technisch Physische Dienst; T.N.O. en T.H.; H. Delft: *Acta cryst.* **1953**, *6*, 359.

[27]   X. Zheng; T. Kawae; H. Yamada; K. Nishiyama; C. Xu: *Phys. Rev. Lett.* **2006**, *97*.

[28]   X. Zheng; M. Hagihala; T. Kawae; C. Xu: *Phys. Rev. B.* **2008**, *77*.

[29]   X. Yuan; Y.-J. Chao; Z.-F. Ma; X. Deng: *Electrochem. Commun.* **2007**, *9*, 2591-2595.

[30]   H. Pröbstle; C. Schmitt; J. Fricke: *J. Power Sources* **2002**, *105*, 189-194.

[31]   J. L. Figueiredo; M. F. R. Pereira; P. Serp; P. Kalck; P. V. Samant; J. B. Fernandes: *Carbon* **2006**, *44*, 2516-2522.

[32]   R. N. Reddy; R. G. Reddy: *J. Power Sources* **2003**, *124*, 330-337.

[33]   T. Takei; Y. Yonesaki; N. Kumada; N. Kinomura: *J. Cream. Soc. Jpn.* **2009**, *117*, 1180-1185.

[34]   Z. Lu; D. D. MacNeil; J. R. Dahn: *Electrochem. Solid-State Lett.* **2001**, *4*, A200.

[35]   G. Yang; C. Xing; W. Hirohama; Y. Jin; C. Zeng; Y. Suehiro; T. Wang; Y. Yoneyama; N. Tsubaki: *Catalysis Today* **2013**, *215*, 29-35.

[36]   L. Shao; J. Shu; M. Lao; X. Lin; K. Wu; M. Shui; P. Li; N. Long; Y. Ren: *J. Power Sources* **2014**, *272*, 39-44.

[37]   Y. Sun; X. Hu; W. Luo; Y. Huang: *J. Phys. Chem. C* **2012**, *116*, 20794-20799.

[38]   A. L. M. Reddy; M. M. Shaijumon; S. R. Gowda; P. M. Ajayan: *Nano Lett.* **2009**, *9*, 1002-1006.

[39]   (a) T. T. Gu, R. E. Jin, Y. Liu*, H. F. Liu, X. L. Weng and Z. B. Wu, *Applied Catalysis B: Environmental*, 2013, 129, 30–38. (b) X. Su; L. Yu; G. Cheng; H. Zhang; M. Sun; L. Zhang; J. Zhang: *Applied Energy* **2014**, *134*, 439-445. (c) Z. Wen; X. C. Wang; S. Mao; Z. Bo; H. Kim; S.M. Cui; G. H. Lu; X. L. Feng and J. H. Chen, *Adv. Mater.* 2012, 24, 5610–5616.

[40]   F. Hao; Z. Zhang; L. Yin: *ACS Appl. Mater. Interfaces* **2013**, *5*, 8337-44.

[41]   W. Y. Li; L. N. Xu; J. Chen: *Adv. Funct. Mater.* **2005**, *15*, 851-857.

[42]   W. M. Chen; L. Qie; Q. G. Shao; L. X. Yuan; W. X. Zhang; Y. H. Huang: *ACS Appl. Mater. Interfaces* **2012**, *4*, 3047-53.

[43]   O. Ghodbane; J. L. Pascal; F. Favier: *ACS Appl. Mater. Interfaces* **2009**, *1*, 1130-9.

[44]   F. Jiao; P. G. Bruce: *Adv. Mater.* **2007**, *19*, 657-660.

[45]   J. Li; S. Xiong; X. Li; Y. Qian: *J. Mater. chem.* **2012**, *22*, 23254.

[46]   K. Cao; L. Jiao; Y. Liu; H. Liu; Y. Wang; H. Yuan: *Adv. Funct. Mater.* **2015**, *25*, 1082-1089.

[47]   K. Z. Cao, L.F. Jiao, Y. C. Liu, H. Q. Liu, Y. J. Wang and H. T. Yuan, *Adv. Funct. Mater.*, 2015, 25, 1082–1089.

[48] Y. M. Sun, X. L. Hu, W. Luo and Y. H. Huang, *J. Mater. Chem.*, 2012, 22, 13826.

[49] C. X. Peng, B. D. Chen, Y. Qin, S. H. Yang, C. Z. Li, Y. H. Zuo, S. Y. Liu and J. H. Yang, *ACS Nano*, 2012, 6, 1074-1081..

[50] Z. A. Zhang, S. F. Jiang, Y. Q. Lai, J. M. Li, J. X. Song and J. Li, *J. Power Sources*, 2015, 284, 95 – 102.

[51] D.W. Wang, F. Li, M. Liu, G. Q. Lu, and H. M. Cheng, *Angew. Chem.Int. Ed.* 2008, 120, 379 –382.

[52]   S. Y. Chung; J. T. Bloking; Y. M. Chiang: *Nat Mater* **2002**, *1*, 123-8.

[53]   J. Shu; R. Ma; L. Shao; M. Shui; D. Wang; K. Wu; N. Long; Y. Ren: *Electrochim. Acta* **2013**, *102*, 381-387.

[54]   Z. Zhang; Z. Li; F. Hao; X. Wang; Q. Li; Y. Qi; R. Fan; L. Yin: *Adv. Funct. Mater.* **2014**, *24*, 2500-2509.

[55] Y. Xu, M. Dunwell, L. Fei, E. Fu, Q. L. Lin, B. Patterson, B. Yuan, S. G. Deng, P. Andersen, H. M. Luo and G. F. Zou, *ACS Appl. Mater. Interfaces* 2014, 6, 20408−20413.

[56] L.L. Xiong, Y.L. Xu, T. Tao, J.B. Goodenough, *J. Power Sources*, 2012, 199, 214-219.

[57] L. B. Chen, K. Wang, X. H. Xie and J. Y. Xie,* *J. Power Sources*, 2007, 174, 538–543.

[58] Y. Ma, C. L. Fang, B. Ding, G. Ji and J. Y. Lee,* *Adv. Mater.*, 2013, 25, 4646-4652.

Figure captions

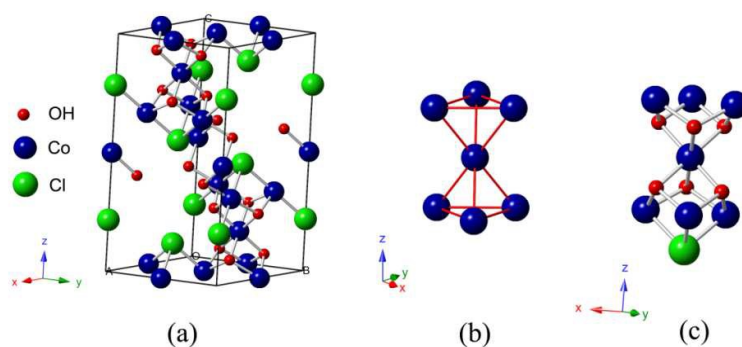Figure 1 (a) The crystal structure of $Co_2(OH)_3Cl$ and (b-c) isolated octahedral.

Figure 2 The XRD patterns of $Co_2(OH)_3Cl$ sample and 2%, 4% and 8%Mn-$Co_2(OH)_3Cl$.

Figure 3 XPS spectra of 4%Mn-$Co_2(OH)_3Cl$ xerogel. (a) survey spectrum, (b) Cl 2p , (c) Co 2p binding and (d) Mn 2p energy spectrum.

Figure 4 (a) Typical FESEM images of 4%Mn-$Co_2(OH)_3Cl$. (c-f) O, Cl, Co, Mn EDX mapping images suggest that all species are homogeneously distributed among the area in (b).

Figure 5 (a) N_2 adsorption-desorption isotherms and (b) pore size distribution of $Co_2(OH)_3Cl$ and 4%Mn-$Co_2(OH)_3Cl$.

Figure 6 (a-b) Low-TEM images of 4%Mn-$Co_2(OH)_3Cl$ sample. (c) A HRTEM lattice image, the inter-spacing of 0.44 nm can be well assigned to d-spacing of (012) plane of $Co_2(OH)_3Cl$. (d) SAED patterns of the sample. The diffraction rings from SAED pattern in Fig. 6d are in good agreement with that of (021), (202), (205), (220),(134) and (226) planes of $Co_2(OH)_3Cl$ phase.

Figure 7 (a) Typical TEM images of 4%Mn-$Co_2(OH)_3Cl$. (b) Co, (c) O, (e) Mn and (f) Cl elemental mapping images.(d) The EDS spectrum of 4%Mn-$Co_2(OH)_3Cl$.

Figure 8 Cyclic voltammetric (CV) curves of the first five cycles for (a) 2%Mn-$Co_2(OH)_3Cl$, (b) 4%Mn-$Co_2(OH)_3Cl$ and (c) 8%Mn-$Co_2(OH)_3Cl$ samples at a scan rate of 0.1 $mV·s^{-1}$ between 0.01–3.0 V. (d-e) The charge-discharge curves between 0.01 and 3.0 V at the current of 100 $mA·g^{-1}$ for 2, 4 and 8%Mn-$Co_2(OH)_3Cl$ samples, respectively.

Figure 9 (a) cycling behavior of the 0, 2%, 4% and 8%Mn-$Co_2(OH)_3Cl$ samples at the current density of 100 mAg^{-1}. (b) Rate capability of the 0, 2, 4 and 8%Mn-$Co_2(OH)_3Cl$ samples at the discharge current between 100 and 1600 mAg^{-1}.

Figure 10 EIS spectra of $Co_2(OH)_3Cl$ and 4%, 8% Mn-$Co_2(OH)_3Cl$ samples.

Figure 1 (a) The crystal structure of pure $Co_2(OH)_3Cl$ and (b-c) isolated octahedral.
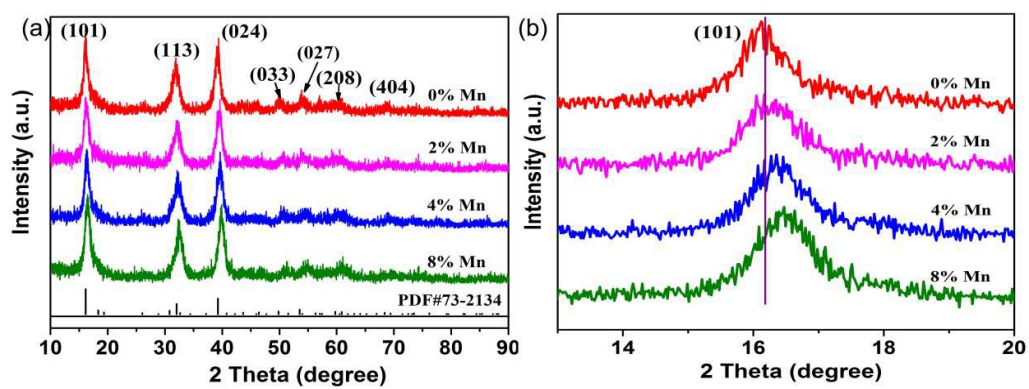
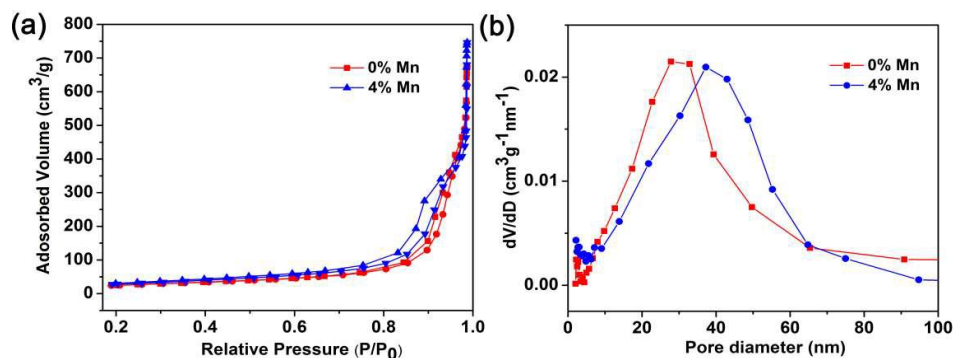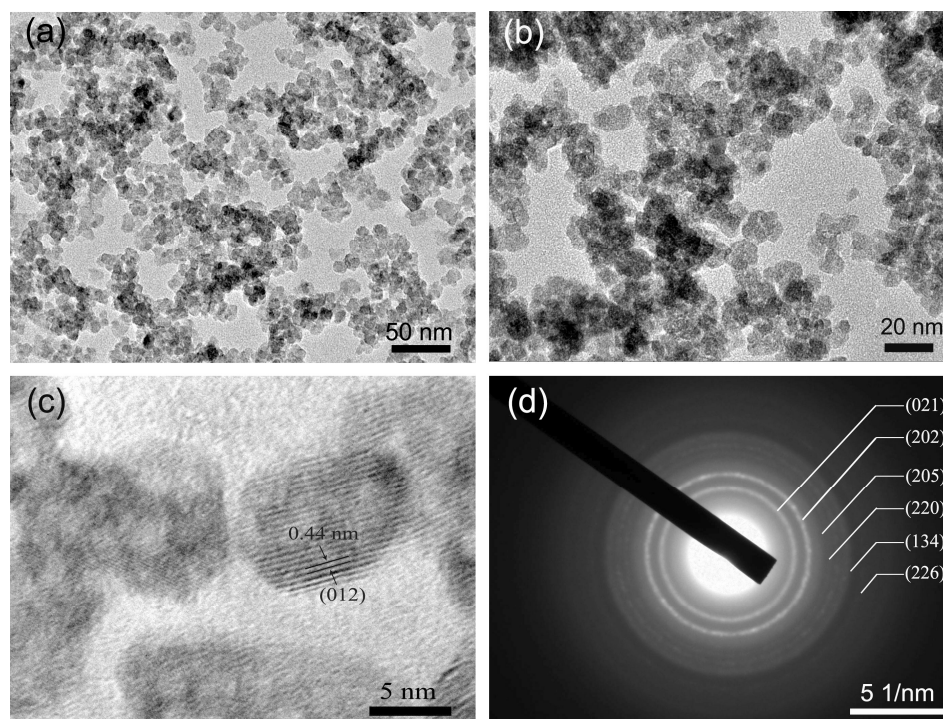**Figure 2** The XRD spectrum of $Co_2(OH)_3Cl$ sample and 2%, 4% and 8%Mn-$Co_2(OH)_3Cl$.
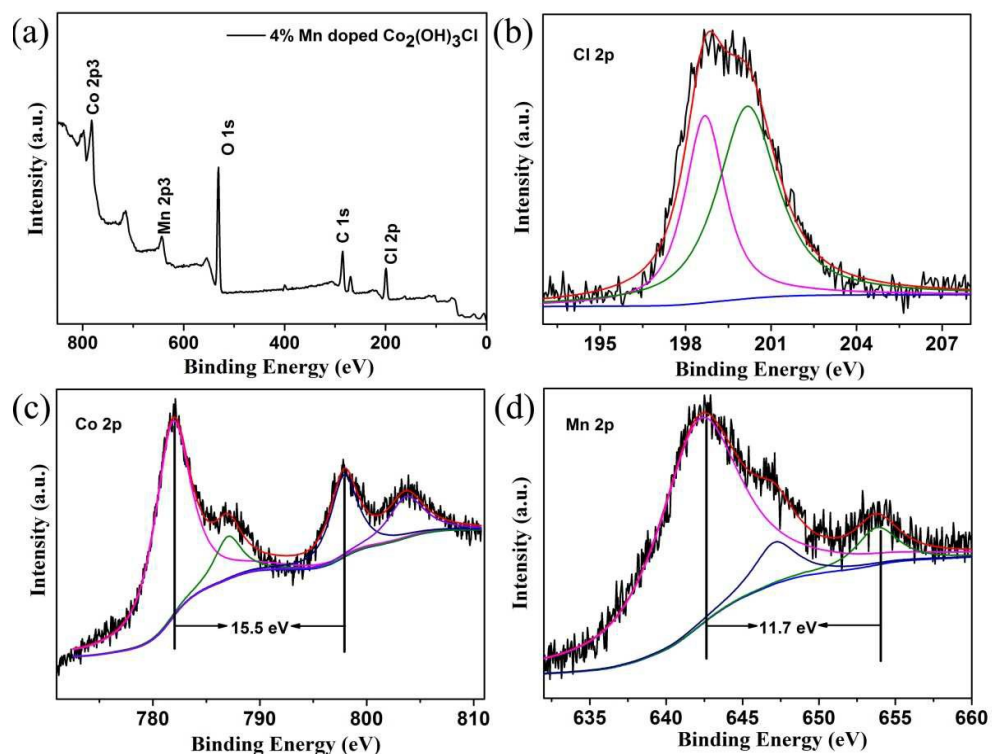
Figure 3 XPS spectra of 4%Mn-Co$_2$(OH)$_3$Cl xerogel: a) survey spectrum, (b) Cl 2p , (c) Co 2p binding and (d) Mn 2p spectrum.
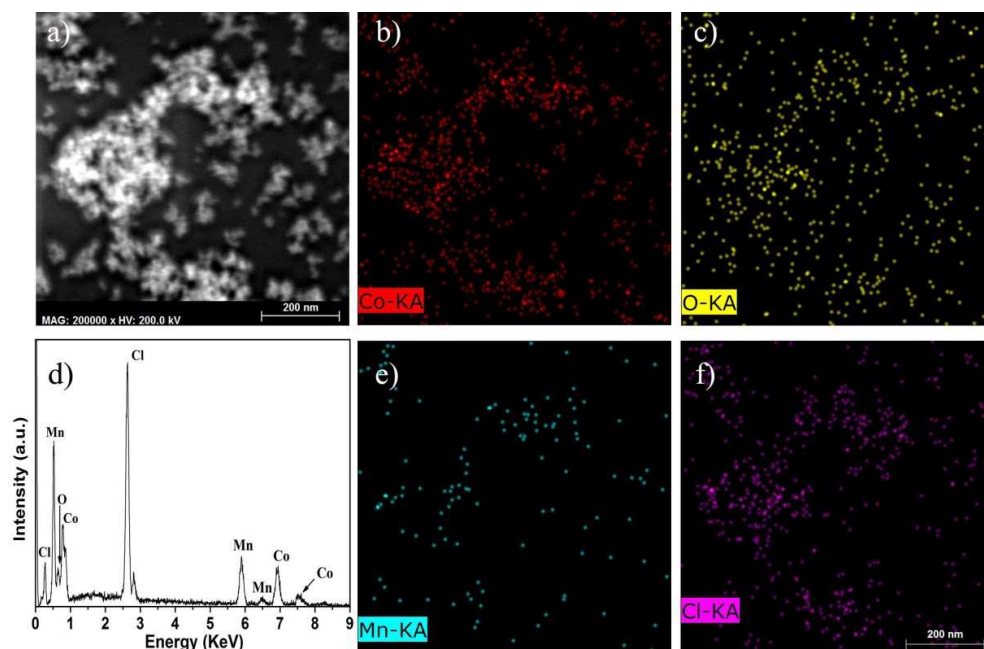

Figure 4 (a) Typical FESEM images of 4%Mn-Co$_2$(OH)$_3$Cl. (c-f) O, Cl, Co, Mn EDX mapping images suggest that all species are homogeneously distributed among the area in (b).
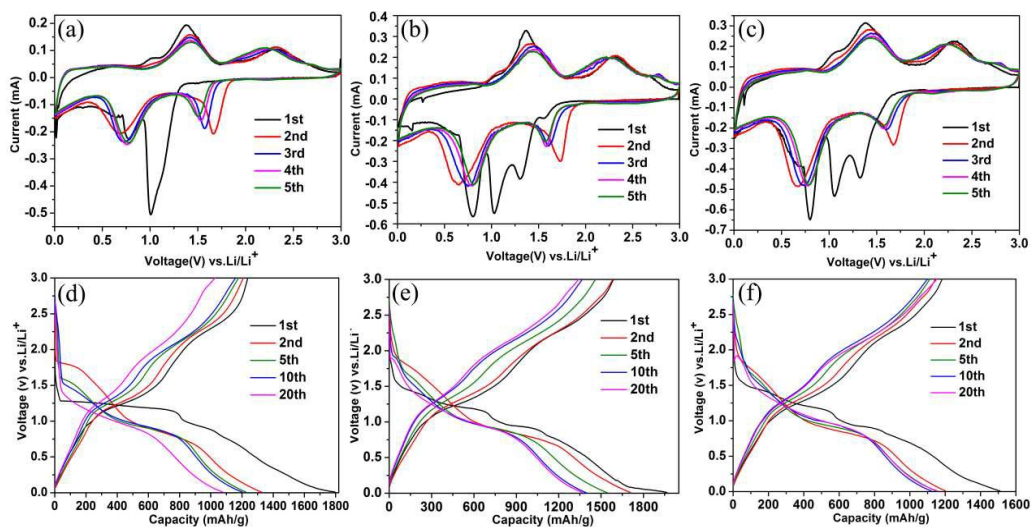
Figure 5 (a) N_2 adsorption-desorption isotherms and (b) pore size distribution of $Co_2(OH)_3Cl$ and 4%Mn-$Co_2(OH)_3Cl$.

Figure 6 (a-b) Low-TEM images of 4%Mn-$Co_2(OH)_3Cl$ sample. (c) A HRTEM lattice image, the inter-spacing of 0.44 nm can be well assigned to d-spacing of (012) plane of $Co_2(OH)_3Cl$. (d) SAED patterns of the sample. The diffraction rings from SAED pattern in Fig. 6d are in good agreement with that of (021), (202), (205), (220),(134) and (226) planes of $Co_2(OH)_3Cl$ phase.
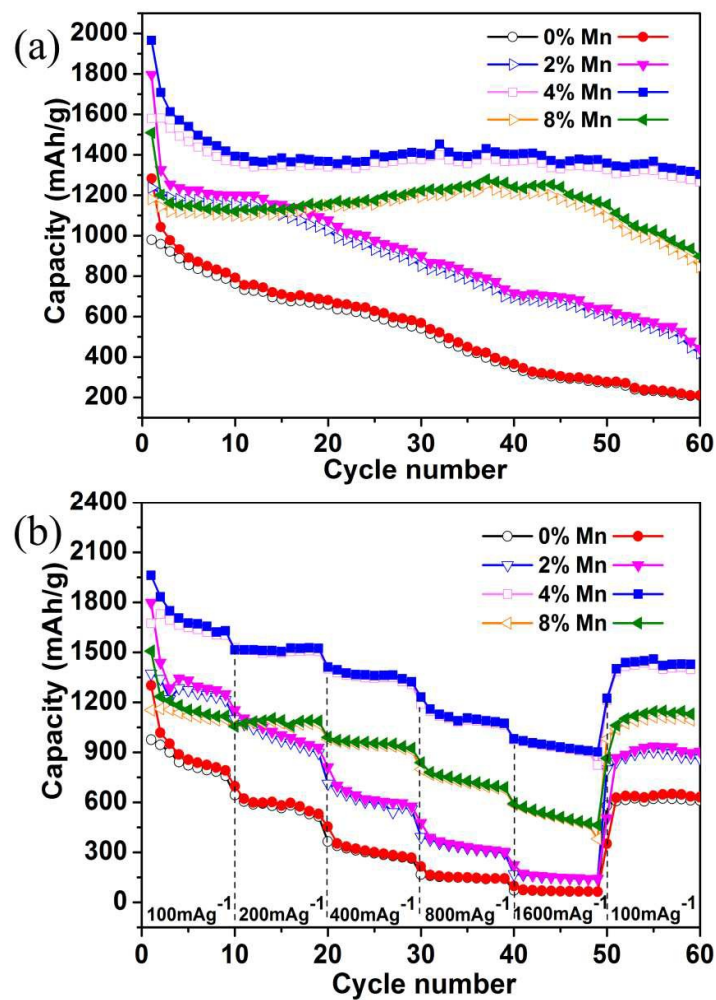
Figure 7 (a) Typical TEM images of 4%Mn-Co$_2$(OH)$_3$Cl. (b) Co, (c) O, (e) Mn and (f) Cl elemental mapping images.(d) The EDS spectrum of 4%Mn-Co$_2$(OH)$_3$Cl.

Figure 8 Cyclic voltammetric (CV) curves of the first five cycles for (a) 2%Mn-Co$_2$(OH)$_3$Cl, (b) 4%Mn-Co$_2$(OH)$_3$Cl and (c) 8%Mn-Co$_2$(OH)$_3$Cl samples at a scan rate of 0.1 mV·s^{-1} between 0.01–3.0 V. (d-e) The charge-discharge curves between 0.01 and 3.0 V at the current of 100 mA·g^{-1} for 2, 4 and 8%Mn-Co$_2$(OH)$_3$Cl samples, respectively.

Figure 9 (a) cycling behavior of the 0, 2, 4 and 8%Mn-Co$_2$(OH)$_3$Cl samples at the current density of 100 mAg^{-1}. (b) Rate capability of the 0, 2, 4 and 8%Mn-Co$_2$(OH)$_3$Cl samples at the discharge current between 100 and 1600 mAg^{-1}.
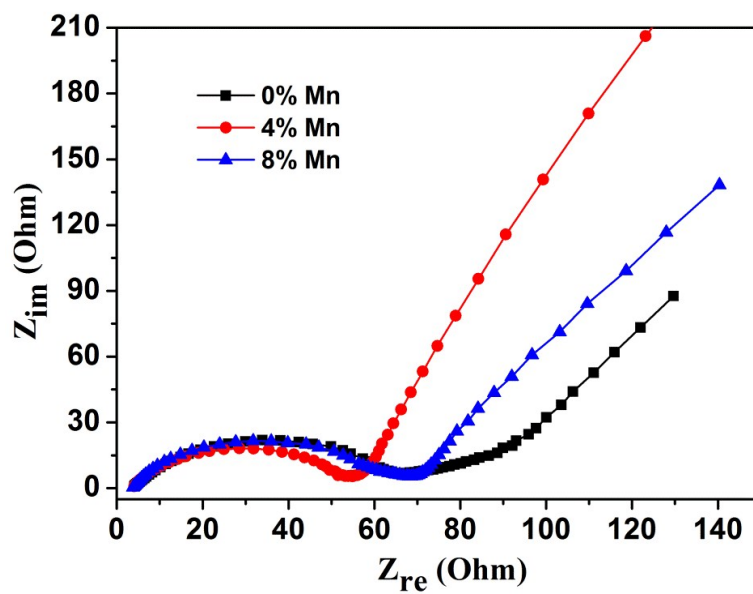
Figure 10 EIS spectra of $Co_2(OH)_3Cl$ and 4%, 8% Mn-$Co_2(OH)_3Cl$ samples.